25th AIAA Applied Aerodynamics Conference, 25–28 June 2007, Hyatt Regency Miami, Miami, Florida

Multidisciplinary Design Exploration of Wing Shape for Silent Supersonic Technology Demonstrator

Kazuhisa Chiba*, Yoshikazu Makino†, and Takeshi Takatoya‡
Japan Aerospace Exploration Agency, Tokyo 182-8522, Japan

Multidisciplinary design exploration with multi objectives has been performed for the wing shape of a silent supersonic technology demonstrator among aerodynamics, structures, and boom noise. Aerodynamic evaluation was carried out by solving Euler equations on computational fluid dynamics, and composite structural evaluation was performed by using NASTRAN for strength and vibration requirements on computational structural dynamics. The intensity of sonic boom was evaluated by a modified linear theory. The optimization problem had five objective functions as the minimizations of the pressure/friction drags and the boom intensity at supersonic condition, and the composite structural weight as well as the maximization of the lift at subsonic low speed condition. The three-dimensional wing shape defined by 58 design variables was optimized on particle swarm optimization and genetic algorithm hybrid method. In the structural evaluation, the combination optimization of stacking sequences of laminated composites was performed for inboard and outboard wings with strength and vibration requirements. Consequently, 75 non-dominated solutions were obtained. Moreover, data mining was performed to obtain the design knowledge for deciding a compromise solution. The data mining revealed the knowledge in the design space, such as the tradeoff information among the objective functions, and the correlations between objective functions and design variables. A compromise solution was successfully determined by using the obtained design knowledge.

I. Introduction

Since the flight experiment of the non-powered supersonic experimental scaled airplane NEXST-1 was succeeded in October 2005[1], the silent supersonic technology demonstrator (S^3TD) then has been researching and developing as a next step in Japan Aerospace Exploration Agency (JAXA)[2]. The initial 0th shape of S^3TD was already designed to focus on low boom and low pressure drag. However, its shape has insufficient performace regarding lift at low speed. Therefore, the second shape with a primary purpose of lift-performance improvement is re-designed to keep low boom intensity(the first shape was for minor change to re-design low-boom geometry). One of the views of this demonstrator is to design using multidisciplinary design optimization (MDO) system.

In the past multi-objective aerodynamic optimization for a supersonic transport (SST)[3], the wing with large sweepback angle was generated to reduce the drag and boom intensity as well as to maintain the lift. However, its wing is not practically designed because of no consideration regarding structures. No matter how an single disciplinary optimization is performed, there is insufficient knowledge to make use of a practical design. That is, multidisciplinary exploration is needed to design and develop a practical aircraft.

As a multi-objective (MO) problem has tradeoffs as an optimum set (called as Pareto-optimal solutions or non-dominated solutions), an MO optimization should be performed to identify such tradeoffs efficiently. MO evolutionary algorithms (MOEAs) were applied to MO optimizations to sample multiple non-dominated solutions because evolutionary algorithms (EAs) sought optimum solutions in parallel using a population of design candidates. In this study, the hybrid method between MO particle swarm optimization (PSO) and adaptive range MOGA was applied to a large-scale and real-world problem to search both global and local optimum solutions efficiently.

*Project Researcher, Aviation Program Group. Member AIAA.
†Senior Researcher, Aviation Program Group. Member AIAA.
‡Senior Researcher, Aviation Program Group.

Moreover, the design knowledge is acquired from MO optimization result by performing data mining. Data mining is a role of the post-process for MO optimization, and essential for the solving of MO optimization. Although design optimization problems are important for engineering, the most important point is the extraction of the knowledge in design space from optimization result. The result obtained by MO optimization problem using EAs is not a sole solution but an optimum set. That is, as MO optimization result is insufficient information for practical design because designers need a conclusive shape. Therefore, data mining techniques can be applied to efficiently obtain fruitful design knowledge. As the combination between the optimization and data mining is a sequence process, it is called as multidisciplinary design exploration (MDE) instead of MDO in the present study. Although the previous MDE was performed for a transonic regional jet aircraft[4], this MDE system had two problems which the wing planform was fixed, and no composite material was considered. Its MDE was dominated by aerodynamics due to these problems.

The objective of the present study is to perform the practical MDE for the S^3TD airplane, *i.e.*, to optimize the three-dimensional wing shape for the S^3TD airplane using computational fluid dynamics (CFD) and computational structural dynamics (CSD) evaluation tools, on a PSO/GA hybrid method. Especially, wing planform is design to improve lift performance and also to restrain low boom performance. Moreover, the design knowledge for S^3TD airplane is obtained by using data mining, a compromise solution is then determined through the designers' discussion using the design knowledge.

II. Multidisciplinary Design Optimization

A. Objective Functions

The following five objective functions were defined. First three objective functions are for aerodynamics, fourth is for hoise, and last is for structures.

1. The minimization of the pressure drag at supersonic cruising condition: $S \cdot C_{D_p}$ (Mach number of 1.6, altitude of 16km, and target C_L of 0.132 for the 0th shape of S^3TD. $S \cdot C_L^{\text{supersonic}} = \text{const.}$ S denotes the one-sided wing reference area.

2. The minimization of the friction drag at supersonic condition: $S \cdot C_{D_f}$.

3. The maximization of the lift at subsonic condition: $S \cdot C_L$ (Mach number of 0.2 and angle of attack of 10.0deg).

4. The minimization of sonic boom intensity I_{boom} at supersonic condition. This objective function value was defined as $|\Delta P_{\max}| + |\Delta P_{\min}|$ at the location with largest peak of sonic-boom signature across boom carpet.

5. The minimization of a composite structural weight W_c for wing using fiber angle of ply and a number of ply with the fulfillment of the strength and vibration requirements.

B. Constraints

As the objective functions were defined to have tradeoff relations, no constraint for flight condition was considered. The geometrical constraints were considered for wing shape definition. The ridge line between wing and fuselage should be extracted. Moreover, the chord length c should satisfy $c_{\text{root}} > c_{\text{kink}} > c_{\text{tip}}$. In addition, the constraint of maximum thickness at each spanwise location is considered. When an individual corresponds to a constraint, another individual is generated because the individual cannot take form as an airplane. This operation is run over until the provided population size is set.

C. Geometry Definition

The design variables were related to planform, airfoil shape, wing twist, and position relative to the fixed fuselage on the 0th shape. A wing planform with a kink was determined by seven design variables as shown in Fig. 1. Airfoil shapes were defined at the wing root, kink, and tip using thickness distributions and camber lines. The thickness distributions were described by Bézier curves using nine control points with 10 design variables, and linearly interpolated in the spanwise direction. The camber line distributions were parameterized using Bézier curves with four control points with four design variables, and incorporated linearly in the spanwise direction. Wing twist was represented by using B-splines using six control points with six design variables. The twist position was 80% chordwise location so that the straight hinge line for aileron was secured. The position of the wing root relative to the fuselage was parameterized by z coordinate of the leading edge, angle of attack, and dihedral. The entire computational geometry was thus defined by using 58 design variables summarized in Table 1. Although the S^3TD has the components of fuselage, main wing, engine, and tail wing, the wing-body configuration was considered shown in Fig 2. In the present study, a robust surface mesh was automatically generated in the following steps; a) generation of the wing geometry, b) extraction of the intersection line between the body and wing, c) deletion of the wing geometry which is inside the body, and they are united, d) generation of the mesh point distributions along created ridges, and e) generation of unstructured surface mesh using advancing front method[5,6].

Table 1. Detail of design variables.

serial number	*correspondent design variable*	
1, 2	span length	inboard, outboard
3 - 5	chord length	root, kink, tip
6, 7	sweepback angle	inboard, outboard
8	z coordinate	root leading edge
9	angle of attack for attachment to fuselage	
10	dihedral angle	
11 - 22	camber control points	root, kink, tip
23 - 52	thickness control points	root, kink, tip
53 - 58	twist control points	

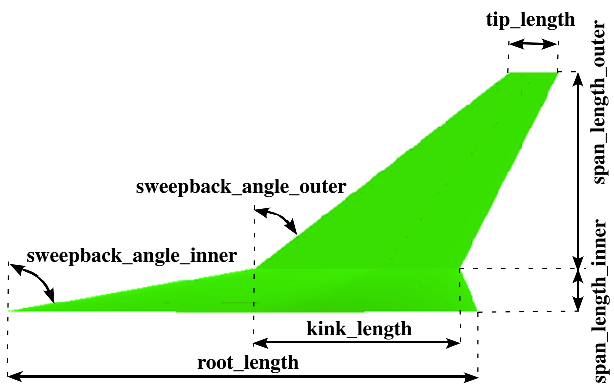

Figure 1. Wing planform definition using seven design variables.

D. Optimizer

A hybrid method between PSO[7,8] and GA[9,10] was employed. Recent optimization work often uses a response surface model(RSM) based on kriging surrogate model to restrain evaluation time[11–13]. However, when the problem with many design variables is considered, the many initial sample points are needed to maintain the accuracy of response surface[14] (10 times number of design variables is generally needed for initial sample points). In the present study, RSM is not selected to avoid the problem of large evaluation time for initial samples.

GAs have generally not for a capability to search local optima but for a faculty of global search. On the other hand, PSO is efficient to search for local optima because it deals with the coordinates of design variables directly. The hybridization between them may produce both capabilities. As PSO and GA use mutation (called as perturbation in PSO) for the maintenance of solution diversity and the prevention of

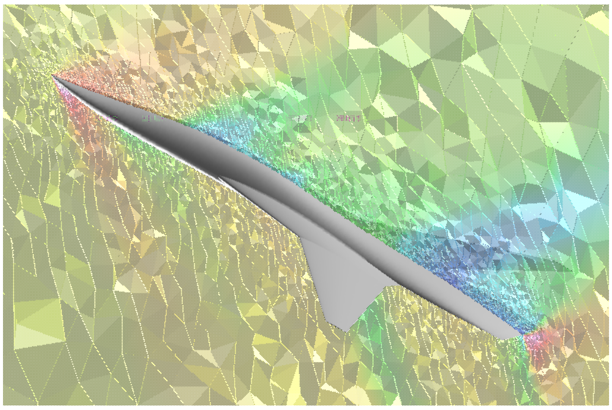

Figure 2. 0th shape without engine and tail wing on unstructured mesh colored by the pressure distribution.

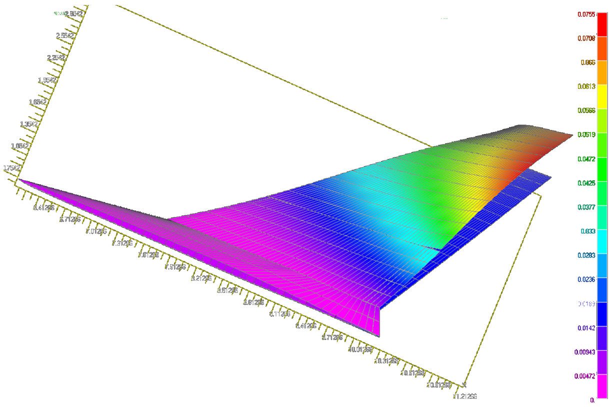

Figure 3. Deformed shape of 0th shape colored by the displacement for height direction.

convergence to a local optima, the convergence to Pareto solutions becomes worse. The PSO/GA hybrid method improves of diversity and enriches the quality of the obtained solutions. It is notable that PSO means MOPSO, GA denotes adaptive range MOGA (ARMOGA) in this study.

1. Particle Swarm Optimization

The PSO method evolved from a simple simulation model of the movement of social groups such as birds and fish, in which it was observed that local interactions underlie the group behavior and individual members of the group can profit from the discoveries and experiences of other members. PSO is the algorithm using plural points such as GA. PSO learns the personal best $\boldsymbol{P}_{\text{best}}$ for exploiting the best results found sofa by each of the particles, and the global best $\boldsymbol{G}_{\text{best}}$ found so fa by the whole swarm for encouraging further exploration and information sharing between the particles. In PSO, each solution (particle) $\boldsymbol{x}_n$ in the swarm of N particles is endowed using the following equations.

$$\boldsymbol{x}_n^{(t+1)} = \boldsymbol{x}_n^{(t)} + \chi \boldsymbol{v}_n^{(t)} + \boldsymbol{\epsilon}^{(t)} \tag{1a}$$

$$\boldsymbol{v}_n^{(t+1)} = w\boldsymbol{v}_n^{(t)} + c_1 r_1 (\boldsymbol{P}_{\text{best}n} - \boldsymbol{x}^{(t)}) + c_2 r_2 (\boldsymbol{G}_{\text{best}n} - \boldsymbol{x}^{(t)}) \tag{1b}$$

where $\chi \in [0, 1]$ is a constriction factor which controls the velocity's magnitude. w, c_1, and c_2 are parameters. r_1 and r_2 are two uniformly distributed random numbers in the range $[0, 1]$. t denotes the searching cycle which is similar to the generation in GA. n denotes each individual. $\boldsymbol{x}$ is the vector for design variable, and $\boldsymbol{v}$ denotes the velocity vector. $\boldsymbol{\epsilon}$ denotes perturbation. Although original PSO introduces a normal perturbation, a Laplacian density $p(\epsilon) \propto \exp(-|\epsilon|/0.1)$ is used in the present study. The Laplacian distribution yields occasional large perturbations enabling wider exploration.

2. Multi-Objective PSO

The MOPSO is developed by using the method proposed by Alvarez-Banitez *et al*[8]. The determination manner of $\boldsymbol{P}_{\text{best}}$ and $\boldsymbol{G}_{\text{best}}$ is essential, because the result of MO problem has plural optimum solutions. Especially, the determination of $\boldsymbol{G}_{\text{best}}$ is important. In this study, the manner is employed which determines the $\boldsymbol{G}_{\text{best}}$ based on the Pareto dominance concepts.

The non-dominated solutions for exploration are held as the archive A. X_a and A_x define as $X_a \equiv \{x \in X | a \prec x\}$ and $A_x \equiv \{a \in A | a \prec x\}$, respectively. $\boldsymbol{G}_{\text{best}}$ is determined by using X_a as follows;

$$\boldsymbol{G}_{\text{best}n} = \begin{cases} a \in A \quad \text{with probability} \propto |X_a|^{-1} & \text{if} \quad x \in A \\ a \in A_X \, \text{with probability} \propto |X_a|^{-1} & \text{otherwise} \end{cases} \tag{2}$$

P_{best} is updated unless the present position is dominated by the position of last generation.

3. *Operators for GA*

The real-coded MOGA was used in this study because the value of design variables is directly employed for the chromosome of individual. Regarding crossover, the blended crossover method (BLX-α)[15], and the principal component analysis-BLX-α method (PCA-BLX-α)[16] were used, and then the quarter of the population size was assigned to each crossover method. The other population was assigned to PSO. When the mutation rate is high, an EA search is close to a random search and results in slow convergence. Therefore, the mutation rate was defined by using the inverse of the number of design variable in this study.

E. Evaluation Method

The present exploration system prepared two evaluation modules for aerodynamics, structures, and boom noise. As the structures module used the result of aerodynamic evaluation, these phases were carried out one by one. The master processing element (PE) managed PSO/GA, while the slave PEs computed aerostructural evaluation processes. Slave processes did not require synchronization. It took roughly seven days at least to evaluate one generation.

1. *Aerodynamic Evaluation*

In the present study, TAS-Code, parallelized unstructured Euler/Navier-Stokes solver using domain decompositions and message-passing interface (MPI) library, was employed to evaluate $S \cdot C_{D_p}$ and $S \cdot C_L$. The three-dimensional Euler equations were solved with a finite-volume cell-vertex scheme on the unstructured mesh[5]. The Harten-Lax-van Leer-Einfeldt-Wada Riemann solver[17] was used for the numerical flux computations. The Venkatakrishnan's limiter[18] was applied when reconstructing the second order accuracy. The lower-upper symmetric-Gauss-Seidel implicit scheme[19] was applied for time integration.

Euler computations were performed under subsonic and supersonic flight conditions, respectively. Taking advantage of the parallel search in PSO/GA, the present optimization was parallelized. Moreover, the CFD computation was also parallelized on the scalar machine.

The following Prandtle-Hoerner's equation was used for the estimation of $S \cdot C_{Df}$ to avoid huge computational time due to Navier-Stokes computation.This empirical equation is often employed for practical designs in business.

$$\begin{aligned} C_{D_f} &= C_f(Re, M) \cdot \frac{S_{\text{wet}}}{S_{\text{ref}}} \\ &= \frac{0.455}{(\log_{10} Re)^{2.58}} \cdot (1 + 0.15M^2)^{-0.58} \cdot \frac{S_{\text{wet}}}{S_{\text{ref}}} \end{aligned} \tag{3}$$

2. *Structural Evaluation*

In the present MDE system, structural optimization of a wing stacking sequences of laminated composites was performed to realize minimum W_c with constraints of strength and vibration requirements. The vibration requirement was defined instead of flutter one. Given the wing outer mold line for each individual, finite element model (FEM) was generated from aerodynamic evaluation result of supersonic cruising condition, such as coordinates, pressure coefficient, and normal vector (x, y, z, C_p, x_{normal}, y_{normal}, and z_{normal}) shown in Fig. 3. The strength and vibration characteristics were evaluated by using the commercial software MSC. NASTRAN$^{\text{TM}}$. Wing had inner and outer boards. Inboard wing was composed of multi-frame structure, such as frame, rib, and spar. Outboard wing compounded from full-depth honeycomb sandwich structure.

The design variables were six, such as stacking sequences (fiber angle of a ply θ and number of ply n) of the skin in outboard wing, the skin in inboard wing, and the frames in inner wing. θ was defined as symmetrical stacking $[0/\theta/-\theta/90]_{ns}$. It is notable that n is set on $^{\forall}n \in \boldsymbol{N} \leq 25$. When n was greater than 25, the individual cannot fulfill the structural requirements. A rank has penalty in the optimizer. Note that θ was set on 15, 30, 45, 60, and 75degs.

First, strength analysis was carried out until six design variables fulfill the strength requirement at each node of FEM mesh on each stacking sequences. Then, oscillation analysis was performed using the combinations of the design variables satisfied with the strength requirement until they fulfill the vibration requirements (greater than 8Hz for bending-first-mode and also greater than 50Hz for twist-first-mode). The computational condition was set on the symmetrical maneuver +6G and the margin of safety was set on 1.25. The speed of sound and the air density was set under the condition of altitude of 16km.

3. Sonic Boom Evaluation

The computer-aided design(CAD)-based Automatic Panel Analysis System (CAPAS) was used to evaluate I_{boom}. CAPAS was a conceptual aerodynamic design tool in JAXA. This tool comprised four design processes as follows; 1) geometry definition of airplane component, 2) combination of all components in an airplane configuration using an application program interface (API) for the CATIA$^{\text{TM}}$V4, 3) generation of panel and aerodynamic analysis using panel method, 4) sonic-boom analysis using a modified linear theory. As an aerodynamic evaluation module in CAPAS was a low-fidelity because a geometry was inaccurate due to rough computational panel, the aerodynamic performance in CAPAS was used only to evaluate I_{boom}.

III. Optimization Results

The population size was set on 16. It took roughly six hours of CPU time of JAXA's super computer system 20 PEs for an Euler computation. The total evolutionary computation of 12 generations was performed, and 75 non-dominated solutions were obtained. Here, the derived non-dominated solutions are focused because a compromise solution is selected from them. The evolution might not converge yet. However, the result was satisfactory because several non-dominated solutions achieved improvements over the 0th shape. Furthermore, sufficient number of solutions was searched so that data mining of the design space can be performed. This can provide useful knowledge for designers.

Figure 4 shows the non-dominated solutions projected on two-dimensional plane between two objectives. This figure indicates the following tradeoff information. There are tradeoffs between $S \cdot C_L$ and W_c. Especially, there are severe tradeoffs between $S \cdot C_{D_p}$ and $S \cdot C_L$, and $S \cdot C_{D_f}$ and $S \cdot C_L$. Whereas, there is no tradeoff between $S \cdot C_{D_p}$ and $S \cdot C_{D_f}$. The relations are obscure between the other combinations of the objective functions. This figure shows that the 0th shape is one of the non-dominated solutions, and it is on the edge of the objective-function space. Because two values of design variables to describe 0th shape, such as the span length and sweepback angle of inboard wing, are near the edge of the defined design space. As several non-dominated fronts are regrettably obscure, data mining deals with the correlations among the objectives.

A. Comparison among the Extreme Solutions regarding the Objective Functions

There are three extreme solutions, which means the champions for each objectives, named as non-dominated solution(NDS) A, B, and C. NDS-A denotes an individual which $S \cdot C_{D_p}$ and I_{boom} were minimized. NDS-B is an individual which $S \cdot C_{D_f}$ and W_c were minimized. NDS-C is an individual which $S \cdot C_L$ was maximized. It is notable that the individuals without fulfillment of strength/vibration requirements were eliminated from the candidates. The planform shapes are shown in Fig. 5, and their geometrical characteristics are summarized in Table 2. Note that AR, $S^{\text{wetted}}_{\text{wing}}$, and N^{ply} denote the aspect ratio, wetted area of one-side wing, and number of ply (for the skin of outboard wing, the skin of inboard wing, and the multi frames of inboard wing), respectively. AR defines $b^2/(S_{\text{ref}} \cdot 2)$, b is a full span length.

NDS-A shows that a large swept angle of leading edge holds the front boom. Therefore, the minimizations of $S \cdot C_{D_p}$ and I_{boom} are achieved, simultaneously. But, because the eigenvalue of twist first mode becomes low, the ply should be stacked for the skin of inboard wing. NDS-B reveals that the smallest wing area achieves the minimization of $S \cdot C_{D_f}$, and the smallest wing area and the low swept angle of leading edge realize the minimization of W_c. But, as the angle of attack at supersonic cruising condition must be high to secure the target C_L, the separation might be triggered. Furthermore, high landing speed must be also secured because of a small wing area. NDS-C shows that a large wing area achieves the maximization of lift at subsonic condition. But, the drags and W_c become high due to the large wing area. The wing planforms of these solutions indicate that the wing area gives strong effects on the objective functions in this study. The shapes of these extreme solutions show that the optimizer can explore to the edge of the design space, efficiently. Consequently, the extreme solutions cannot design practically, and a compromise geometry will be decided using the knowledge in the design space.

IV. Data Mining

Although a design optimization is important for engineering, the most significant point is the extraction of the knowledge in design space. The results obtained by MO optimization are not a sole solution but an

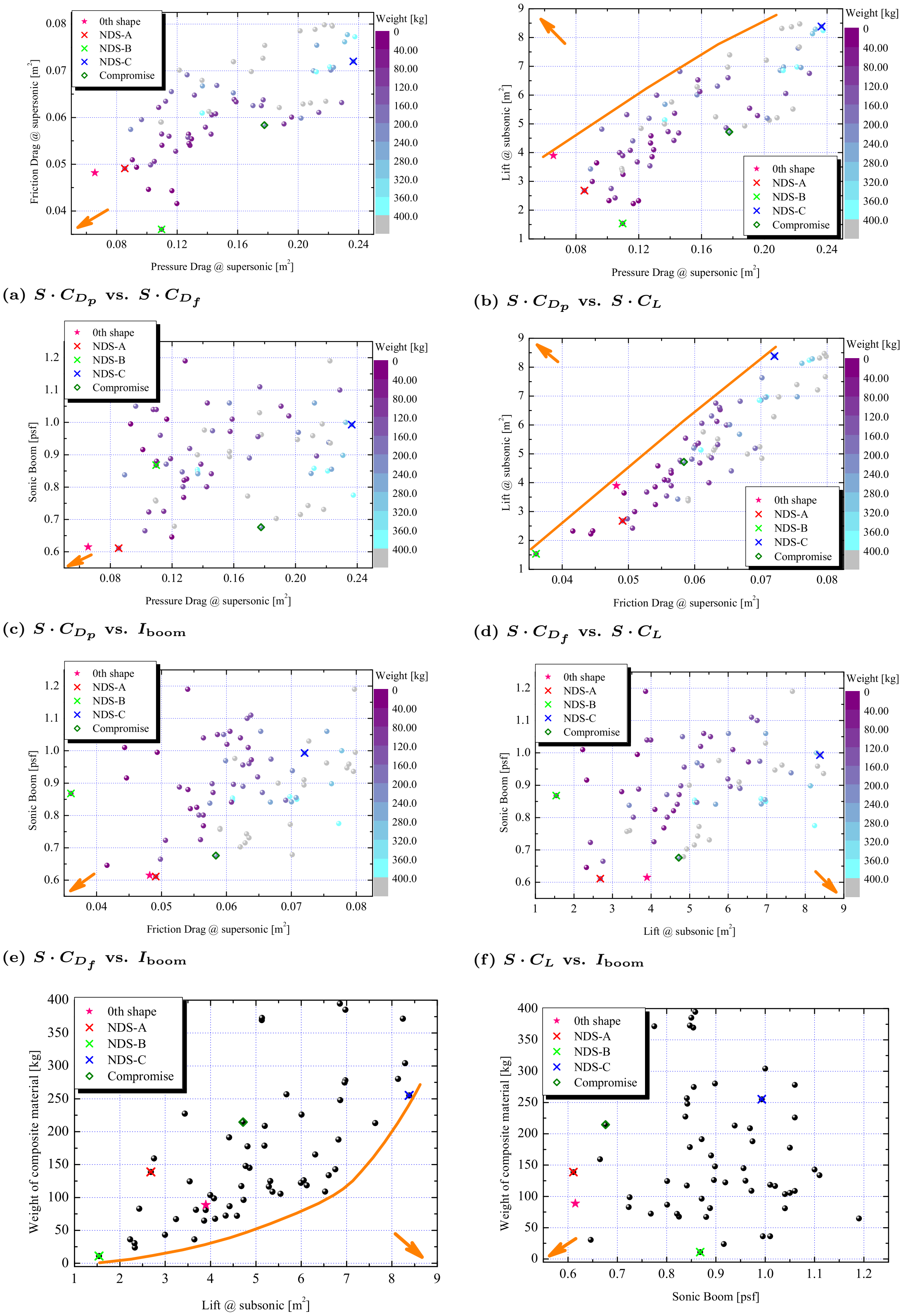

(a) $S \cdot C_{D_p}$ vs. $S \cdot C_{D_f}$

(b) $S \cdot C_{D_p}$ vs. $S \cdot C_L$

(c) $S \cdot C_{D_p}$ vs. I_{boom}

(d) $S \cdot C_{D_f}$ vs. $S \cdot C_L$

(e) $S \cdot C_{D_f}$ vs. I_{boom}

(f) $S \cdot C_L$ vs. I_{boom}

(g) $S \cdot C_L$ vs. W_c

(h) I_{boom} vs. W_c

Figure 4. Derived non-dominated solutions on two dimensional planes between the objective functions. The orange arrow denotes the optimum direction.

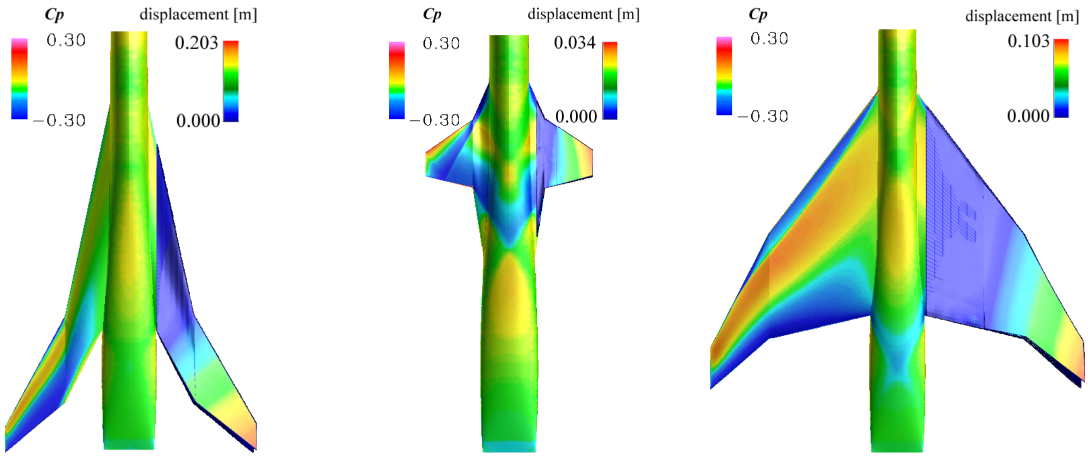

(a) **NDS-A** (b) **NDS-B** (c) **NDS-C**

Figure 5. Comparison among the wing planform of the extreme solutions colored by C_p distribution on CFD and displacement on CSD.

Table 2. Geometrical characteristic values of the extreme solutions.

Individual	$C_{L\,\mathrm{design}}$	α_{cruise}[deg]	AR	$S_{\mathrm{wing}}^{\mathrm{wetted}}$[m^2]	$N^{\mathrm{ply}}_{\mathrm{out\_skin}}/N^{\mathrm{ply}}_{\mathrm{in\_skin}}/N^{\mathrm{ply}}_{\mathrm{in\_rib}}$
NDS-A	0.1300	3.94	2.92	10.81	16/88/32
NDS-B	0.3103	6.85	2.86	4.15	8/24/8
NDS-C	0.0632	1.76	3.08	22.52	56/48/56

optimum set. That is, as multi-objective optimization result is insufficient information for practical design because designers need a conclusive shape. However, the result of MO optimization can be accounted as a hypothetical design database. Data mining as a post-process for an optimization is essential to obtain the fruitful design knowledge efficiently[20–22]. In the present study, functional analysis of variance (ANOVA) and self-organizing map (SOM) were used for data mining technique.

A. Analysis of Variance

ANOVA[23] is one of the data mining techniques showing the effect of each design variable to the objective and the constraint functions in a quantitative manner. ANOVA uses the variance of the model due to the design variables on the approximation function. By decomposing the total variance of model into the variance due to each design variable, the influence of each design variable on the objective function can be calculated. The decomposition is accomplished by integrating out the variables of model $\hat{y}$. $\hat{y}$ denotes an estimated value of unknown function y. The total mean ($\hat{\mu}_{\mathrm{total}}$) and the variance ($\hat{\sigma}^2_{\mathrm{total}}$) of model $\hat{y}$ are as follows:

$$\hat{\mu}_{\mathrm{total}} \equiv \int \cdots \int \hat{y}\left(x_1, x_2, \cdots, x_n\right) dx_1 dx_2 \cdots dx_n \tag{4a}$$

$$\hat{\sigma}^2_{\mathrm{total}} = \int \cdots \int \left[\hat{y}\left(x_1, x_2, \cdots, x_n\right) - \hat{\mu}_{\mathrm{total}}\right]^2 dx_1 dx_2 \cdots dx_n \tag{4b}$$

The main effect of variable x_i and the two-way interaction effect of variable x_i and x_j are given as follows:

$$\hat{\mu}\left(x_i\right) \equiv \int \cdots \int \hat{y}\left(x_1, x_2, \cdots, x_n\right) dx_1 dx_2 \cdots dx_{i-1} dx_{i+1} \cdots dx_n - \hat{\mu}_{\mathrm{total}} \tag{5}$$

$$
\begin{aligned}
&\hat{\mu}_{i,j}\left(x_i, x_j\right) \\
&\equiv \int \cdots \int \hat{y}\left(x_1, x_2, \cdots, x_n\right) dx_1 dx_2 \cdots dx_{i-1} dx_{i+1} \cdots dx_{j-1} dx_{j+1} \cdots dx_n \\
&- \hat{\mu}_i\left(x_i\right) - \hat{\mu}_j\left(x_j\right) - \hat{\mu}_{\text{total}}
\end{aligned} \tag{6}
$$

$\hat{\mu}(x_i)$ and $\hat{\mu}_{i,j}(x_i, x_j)$ quantify the effect of variable x_i and interaction effect of x_i and x_j on the objective function. The variance due to the design variable x_i is obtained as follows:

$$
\hat{\sigma}_{x_i}^2 = \int \left[\hat{\mu}_i\left(x_i\right)\right]^2 dx_i \tag{7}
$$

The proportion of the variance P due to design variable x_i to total variance of model can be expressed by dividing Eq. (7) with Eq. (4b).

$$
\begin{aligned}
P &= \frac{\hat{\sigma}_{x_i}^2}{\hat{\sigma}_{\text{total}}^2} \\
&= \frac{\displaystyle\int \left[\hat{\mu}_i\left(x_i\right)\right]^2 dx_i}{\displaystyle\int \cdots \int \left[\hat{y}\left(x_1, x_2, \cdots, x_n\right) - \hat{\mu}_{\text{total}}\right]^2 dx_1 dx_2 \cdots dx_n}
\end{aligned} \tag{8}
$$

This value indicates[13] the effect of design variable x_i on the objective function $\hat{y}$.

B. Self-Organizing Map

1. General SOM Algorithm

SOM[24] is an unsupervised learning, nonlinear projection algorithm from high to low-dimensional space. This projection is based on self-organization of a low-dimensional array of neurons. In the projection algorithm, the weights between the input vector and the array of neurons are adjusted to represent features of the high dimensional data on the low-dimensional map. The close two patterns are in the original space, the closer is the response of two neighboring neurons in the low-dimensional space. Thus, SOM reduces the dimension of input data while preserving their features.

2. Batch-SOM

In this study, SOMs are generated by using commercial software Viscovery® SOMine 4.0 plus[a] produced by Eudaptics GmbH. Although SOMine is based on the general SOM concept and algorithm, it employs an advanced variant of unsupervised neural networks, *i.e.*, Kohonen's Batch SOM[25,26]. The algorithm consists of two steps that are iterated until no more significant changes occur: search of the best-matching unit c_i for all input data $\{\boldsymbol{x}_i\}$ and adjustment of weight vector $\{\boldsymbol{m}_j\}$ near the best-matching unit. The Batch-SOM algorithm can be formulated as follows:

$$
c_i = \arg\min \|\boldsymbol{x}_i - \boldsymbol{m}_j\| \tag{9a}
$$

$$
\boldsymbol{m}_j^* = \frac{\displaystyle\sum_i h_{jc_i} \boldsymbol{x}_i}{\displaystyle\sum_i h_{jc_i}} \tag{9b}
$$

where $\boldsymbol{m}_j^*$ is the adjusted weight vector. The neighborhood relationship between two neurons j and k is defined by the Gaussian-like function $h_{jk} = \exp(-d_{jk}^2/r_t^2)$. Where d_{jk} denotes the Euclidean distance between the neuron j and the neuron k on the map, and r_t denotes the neighborhood radius which is decreased with the iteration steps t.

The standard Kohonen algorithm adjusts the weight vector after all each record is read and matched. On the contrary, the Batch-SOM takes a 'batch' of data (typically all records), and performs a 'collected' adjustment of the weight vectors after all records have been matched. This is much like 'epoch' learning

[a] "Eudaptics" available online at http://www.eudaptics.com [cited 16 June 2004].

in supervised neural networks. The Batch-SOM is a more robust approach, since it mediated over a large number of learning steps. In the SOMine, the uniqueness of the map is ensured by the adoption of the Batch-SOM and the linear initialization for input data. Much like some other SOMs[27], SOMine creates a map in a two-dimensional hexagonal grid. Starting from numerical, multivariate data, the nodes on the grid gradually adapt to the intrinsic shape of the data distribution can be read off from the emerging map on the grid. The trained SOM is systematically converted into visual information[4, 20].

3. Cluster Analysis

Once SOM projects input space on a low-dimensional regular grid, the map can be utilized to visualize and explore properties of the data. When the number of SOM units is large, to facilitate quantitative analysis of the map and the data, similar units need to be grouped, *i.e.*, clustered. The two-stage procedure — first using SOM to produce the prototypes which are then clustered in the second stage — was reported to perform well when compared to direct clustering of the data[27].

Hierarchical agglomerative algorithm is used for clustering here. The algorithm starts with a clustering where each node by itself forms a cluster. In each step of the algorithm two clusters are merged: those with minimal distance according to a special distance measure, the SOM-Ward distance. This measure takes into account whether two clusters are adjacent in the map. This means that the process of merging clusters is restricted to topologically neighbored clusters. The number of clusters will be different according to the hierarchical sequence of clustering. A relatively small number will be chosen for visualization, while a large number will be used for generation of codebook vectors for respective design variables.

V. Data-Mining Results

Although SOM looks down the global knowledge in design space like a bird-eye view, it has a disadvantage that it is possible to overlook the design knowledge due to a large number of design variables. In this study, data mining by SOM was performed after key design variables were addressed by ANOVA.

A. Knowledge by ANOVA

The variance of the design variables and their interactions by ANOVA are shown in Fig. 6. Their proportions are shown which were larger than 1% to the total variance. It is notable that ANOVA was analyzed to except a individual with great value leap for I_{boom}, and 16 individuals without fulfillment of structural requirements. The symbol 'dv' denotes design variable and '-' means the interaction between two design variables.

Figure 6a shows that dv25, dv14, dv1, and dv6 give the effect on $S \cdot C_{D_p}$. Dv25 describes the leading-edge bluntness at root. As the wing thickness at root is largest due to the long chord length, the leading-edge bluntness at root is most effective on $S \cdot C_{D_p}$. Dv14 represents the height of rearward camber at root. Dv14 decides the angle which the flow takes on the rearward wing. As the curvature of camber line becomes large when the value of dv14 becomes high, $S \cdot C_{D_p}$ increases. Dv1 describes the inboard span length. As wetted area increases when dv1 becomes high, $S \cdot C_{D_p}$ increases.

Figure 6b shows that dv1, dv2, and dv4 give the effects on $S \cdot C_{D_f}$. It reveals that the span length and the chord length at kink are effective to $S \cdot C_{D_f}$. In this study, as the Prandtle-Hoerner's equation gives $S \cdot C_{D_f}$, it becomes high when the individual has a large wetted area. Moreover, in this study, the chord length at root does not fluctuate largely. The design variables represented a large chord length at kink give effects on the increase of the wing area.

Figure 6c reveals that dv1 and dv2 give effects on $S \cdot C_L$. The span length of inboard wing decides the $S \cdot C_L$. The mechanism that $S \cdot C_L$ increases due to the span length is similar to that of $S \cdot C_{D_f}$ increase.

Figure 6d shows that dv6 and dv43 give effects on I_{boom}. The dv6 describes the leading-edge sweepback angle of inner wing. As the I_{boom} at the front boom becomes weak when this angle becomes large, the total of I_{boom} thus decreases.

Figure 6e shows that dv25 and dv16 give effects on W_c. Dv25 describes the leading-edge bluntness at root. As the wing becomes thin near the leading edge when leading edge has sharpness, the strength becomes weak and also the natural frequency becomes low. Since the number of ply should increase to fulfill the structural requirements, W_c increases. Dv16 describes the frontward camber height at kink. The curvature of camber line multiplies strength and increases natural frequency. Camber height gives effect on W_c

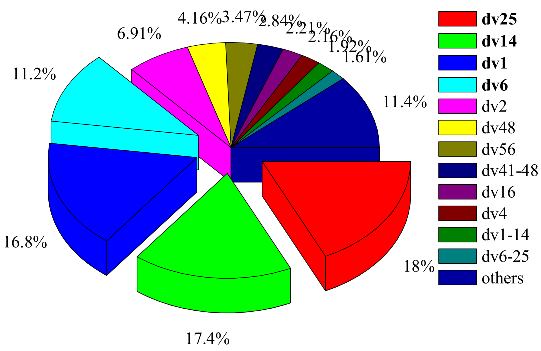

(a) $S \cdot C_{D_p}$

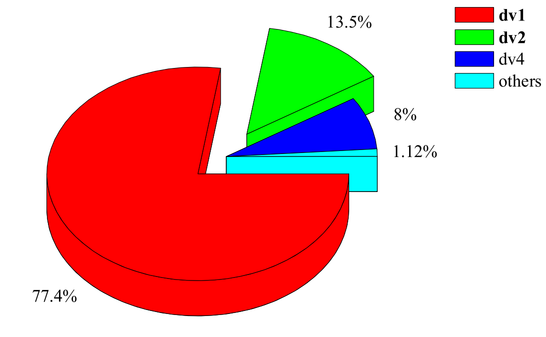

(b) $S \cdot C_{D_f}$

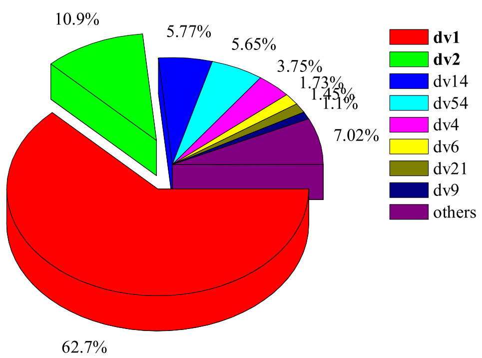

(c) $S \cdot C_L$

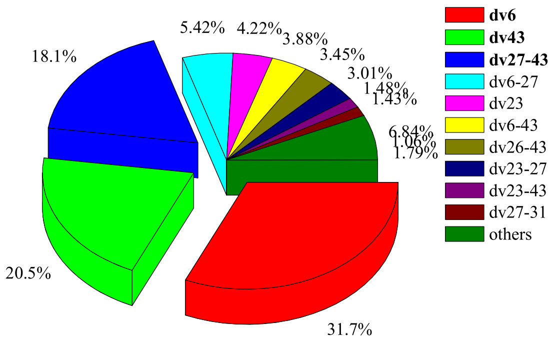

(d) I_{boom}

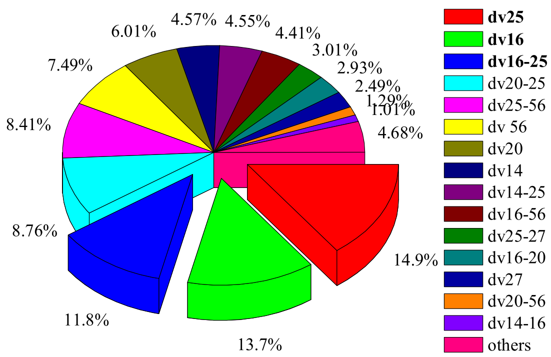

(e) W_c

Figure 6. Proportion of design-variable influence for the objective functions using ANOVA.

B. Knowledge by SOM

The resulting 75 non-dominated solutions have been projected onto the two dimensional map of SOM. Figure 7 shows the colored SOM by the objective functions with 11 clusters taking the five objective functions into consideration. Figure 7a shows that left area collects the designs with high $S \cdot C_{D_p}$, and also right area collects the designs with low $S \cdot C_{D_p}$. Figure 7b shows that upper left area collects the designs with high $S \cdot C_{D_f}$, and also upper right area collects the designs with low $S \cdot C_{D_f}$. Figure 7c shows the similar coloring pattern compared with Fig. 7b. Figure 7d shows that lower right area collects the designs with high I_{boom}. There is no clear pattern regarding low I_{boom}. Figure 7e shows that upper left area collects the designs without fulfillment of the structural requirements, and also right area collects the designs with low W_c. This result is summarized in Fig. 8.

Figure 7 reveals the following tradeoff and correlation information. There is no tradeoff between $S \cdot C_{D_p}$ and $S \cdot C_{D_f}$. On the other hand, there is strong tradeoffs between $S \cdot C_L$ and $S \cdot C_{D_p}$, and $S \cdot C_L$ and $S \cdot C_{D_f}$. There is no correlation between I_{boom} and the other objectives, that is, I_{boom} does not depend on the other objectives in the design space. In this study, there is no tradeoff between $S \cdot C_{D_p}$ and I_{boom} because the fuselage is fixed. The nose geometry is generally effective to the tradeoff between them. There is correlation among W_c and $S \cdot C_{D_p}$, $S \cdot C_{D_f}$, and $S \cdot C_L$ when W_c becomes low. Moreover, since the cluster on the upper right corner in Fig. 7 has low values of all objectives, there is a sweet spot when $S \cdot C_L$ is tolerable. But, the primary objective of this MDO is to improve the lift performace at low speed. The knowledge regarding this sweet sport suggests that the other four objectives are corrupted compared with 0th shape even when any compromise solution improved lift performance at low speed is selected.

Figure 9 shows the SOMs colored by C_{D_p} and C_L. Figure 9a shows that upper right area collects the high C_{D_p}, and upper center area and lower right areas collect the low C_{D_p}. Figure 9b shows that lower left area collects high C_L, and right area collects low C_L, however, the color pattern is unclear. As the comparison among Fig. 7a, 7c, and Fig. 9 shows the different color pattern, the optimum direction disagrees between C_{D_p} and $S \cdot C_{D_p}$, and between C_L and $S \cdot C_L$. When $S \cdot C_{D_p}$ and $S \cdot C_L$ is considered, the optimum direction is dominated by wing area.

The SOMs can be also contoured by 58 design-variable values. Figure 10 shows the SOMs colored by the characteristic design variables addressed by ANOVA. These colored SOMs reveal 'how' design variables operate on the objective functions. Figure 10a shows that left area collects high dv1. Also, upper right area collects low dv1. Therefore, when the span length of inboard wing becomes high, $S \cdot C_{D_p}$, $S \cdot C_{D_f}$, and $S \cdot C_L$ become high, and also when it becomes low, $S \cdot C_{D_p}$, $S \cdot C_{D_f}$, $S \cdot C_L$, and W_c become low. Figure 10b shows that upper left area collects high dv2. Therefore, when the span length of outboard wing becomes high, $S \cdot C_{D_f}$, $S \cdot C_L$, and W_c becomes high. As Fig. 10c shows that upper right area collects high dv6, $S \cdot C_{D_p}$ and I_{boom} becomes low when the sweepback angle of inboard wing becomes high. Figure 10d shows that left area roughly collects high dv14, but this color pattern is insufficient to mention the correlation. Therefore, the rearward camber height at root does not have a large effect on $S \cdot C_{D_p}$. Figure 10e shows that upper center area collects low dv16. Therefore, W_c tends to become high when the frontward camber height at kink becomes low. Figure 10f shows that dv25 does not fluctuate so much and there is no clear contour pattern. Therefore, the leading-edge bluntness at root does not give large effect on the objectives. As Fig. 10g shows that there is incoherent color pattern, there is no correlation between the leading-edge bluntness at tip and I_{boom}.

The color patterns between two or more SOMs give the qualitative effects. SOM needs to be interpreted while the physical meaning of design variables is considered.

C. Decision of a Compromise Solution

The 75 non-dominated solutions are extracted using SOM to determine a compromise solution. The applicable solutions to the following conditions are firstly excluded from 75 non-dominated solutions; 1) The structural requirements are not fulfilled, 2) $S \cdot C_L$ is low, or wing area is low (this means the constraint for the landing speed.), 3) $S \cdot C_{D_p}$ and $S \cdot C_{D_f}$ are impractically large. As a result of this operation, 24 non-dominated solutions as the practical designs are sorted. The SOM is re-generated using derived 24 non-dominated solutions taking the five objective functions into consideration. The derived SOM with the top views of the sorted 24 non-dominated solutions and its colored maps by the objectives are shown in Fig. 11. The compromise solution is determined from these individuals taking the balance of the five objective functions and the low-boom competence as the primary objective of S^3TD into consideration on SOM.

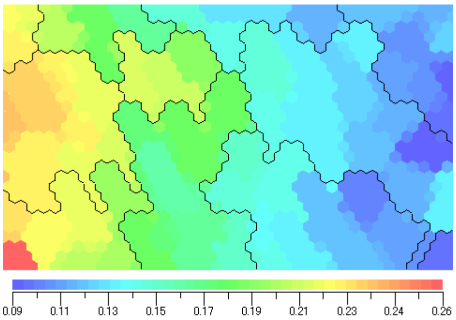

(a) $\boldsymbol{S \cdot C_{D_p}}$

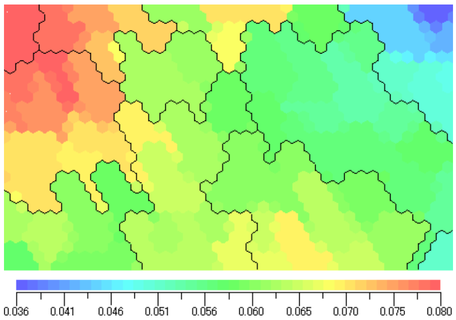

(b) $\boldsymbol{S \cdot C_{D_f}}$

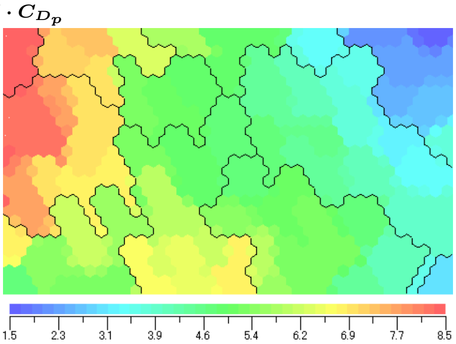

(c) $\boldsymbol{S \cdot C_L}$

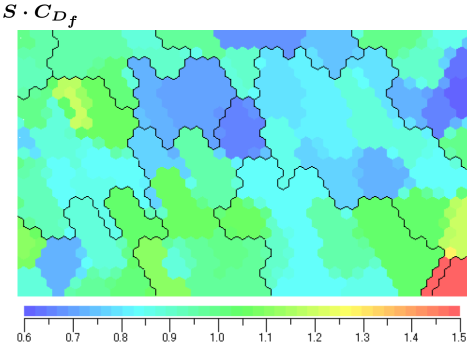

(d) $\boldsymbol{I_{\mathrm{boom}}}$

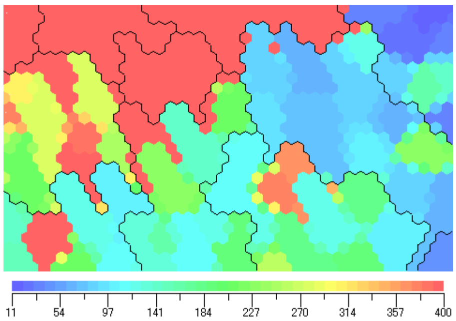

(e) $\boldsymbol{W_c}$

Figure 7. SOMs colored by the objective functions taking the five objective functions into consideration.

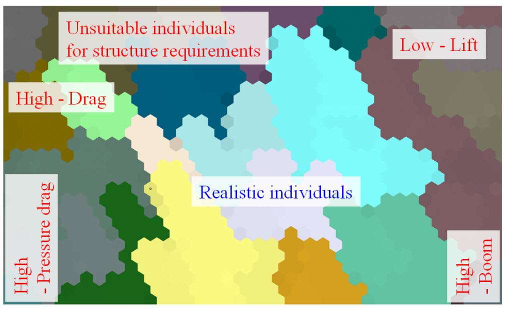

Figure 8. SOM of the derived non-dominated solutions in the five dimensional objective function space. Shadow region denotes that there is impractical individuals for design.

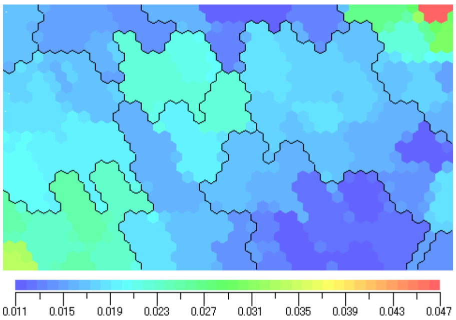

(a) C_{D_p}

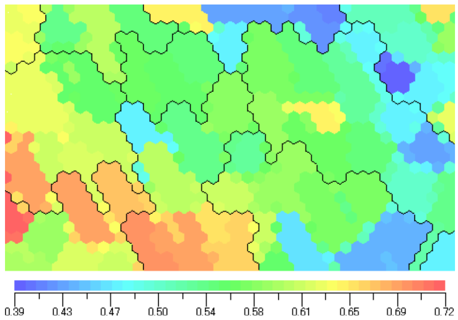

(b) C_L

Figure 9. SOMs colored by the aerodynamic characteristics.

D. Comparison between 0th Shape and Selected Compromise Solution

The comparison of the planform between the 0th shape and the selected compromise solution (called as '*compromise*') is shown in Fig. 12. Also, their airfoils of 0th and *compromise* shapes near the junction relative to the fuselage, kink, and tip are shown. It is notable that 0th shape has no twist and its airfoil is described by NACA64A series. The thickness ratios are respectively defined as 6% at root, 5% at kink, and 3% at tip. The installed angle of wing is -0.5deg relative to the fuselage. 0th shape design was focused on reducing sonic boom. Their characteristics and performance are summarized in Tables 3 and 4. As $S \cdot C_L$ is maximization objective, *compromise* has a larger wing area than that of 0th shape. And, inner wing area of *compromise* becomes large to secure the structural strength. The sweepback angle has more gentle not to give the effects on I_{boom} so that the wing area and structural strength are also secured. But, the chord length near kink becomes short to achieve low W_c and $S \cdot C_{D_f}$. Therefore, the number of ply increases to augment the eigen frequency. *Compromise* has the supersonic leading edge near root to reduce the effect on I_{boom} of the front boom. Also, *compromise* has the blunt leading edge near kink to improve the strength, eigen frequency, and subsonic aerodynamic performance. Data-mining results show that the sharp leading edge near tip gives effect on I_{boom}. But, the wing area gives strong effect on the objectives. Therefore, the knowledge regarding the airfoil shape is unreliable.

The location in the design space for 0th shape and *compromise* is shown in Fig 4. 0th shape has low $S \cdot C_{D_p}$ and $S \cdot C_L$ due to a small wing area, and it locates on the edge in the design space. Also, it has low I_{boom} due to focusing on low-boom design. *Compromise* locates low I_{boom} region as well as compromise of the other objectives. These location in Fig. 4 shows the aerodynamic performance strictly depends on the wing area. Figure 13 shows the spanwise distributions of C_L and C_D, and twist angle for 0th and *compromise* shapes. This figure shows that the twist angle of *compromise* on outer wing is large. That is, outboard is not worked as wing, and down force occurs. C_D becomes still larger due to inverted camber line near the kink. As data-mining results reveal that the design variables regarding twist down and inverted camber line give no effects on the objective functions, the re-design of these design variables can improve the aerodynamic performance without corrupting the other objectives. The knowledge regarding the airfoil shape is insufficient. The primary reason is that its effect is weak to the aerodynamic performance compared with the wing planform. The secondary reason is that only a small number of the generations was performed.

The boom intensity as the primary objective function is finally compared between 0th and *compromise*. Figure 14 shows their ground pressure signatures. Although I_{boom} performance of 0th shape is better, *compromise* also keeps non-N-shaped signature to restrain the initial peak. *Compromise* has better performance of $S \cdot C_L$ for the constraint of landing speed as well as the restraint of I_{boom}. In this study, the rearward boom intensity cannot be discussed because the assumed fuselage-wing configuration ignores an engine nacelle and vertical/horizontal tail wings. But, CFD visualization of C_p distribution on symmetrical plane shown in Fig. 15 reveals that shock wave occurs in the vicinity of wing trailing edge. It is necessary that the full configuration is optimized to design the geometry restrained rearward boom intensity and to obtain the design knowledge regarding cross section shape.

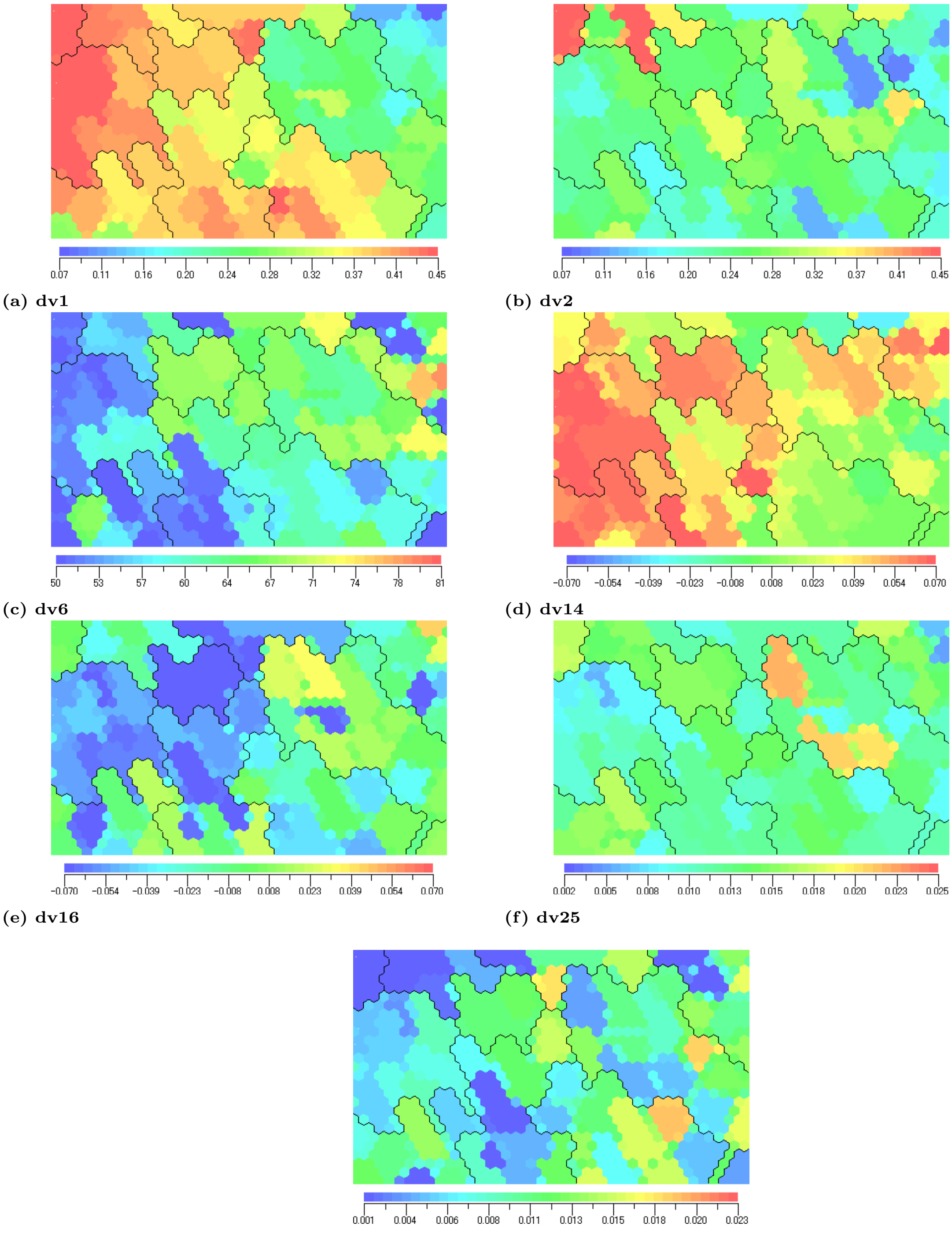

(a) dv1 **(b) dv2**

(c) dv6 **(d) dv14**

(e) dv16 **(f) dv25**

(g) dv43

Figure 10. SOMs colored by the characteristic design variables indicated by ANOVA.

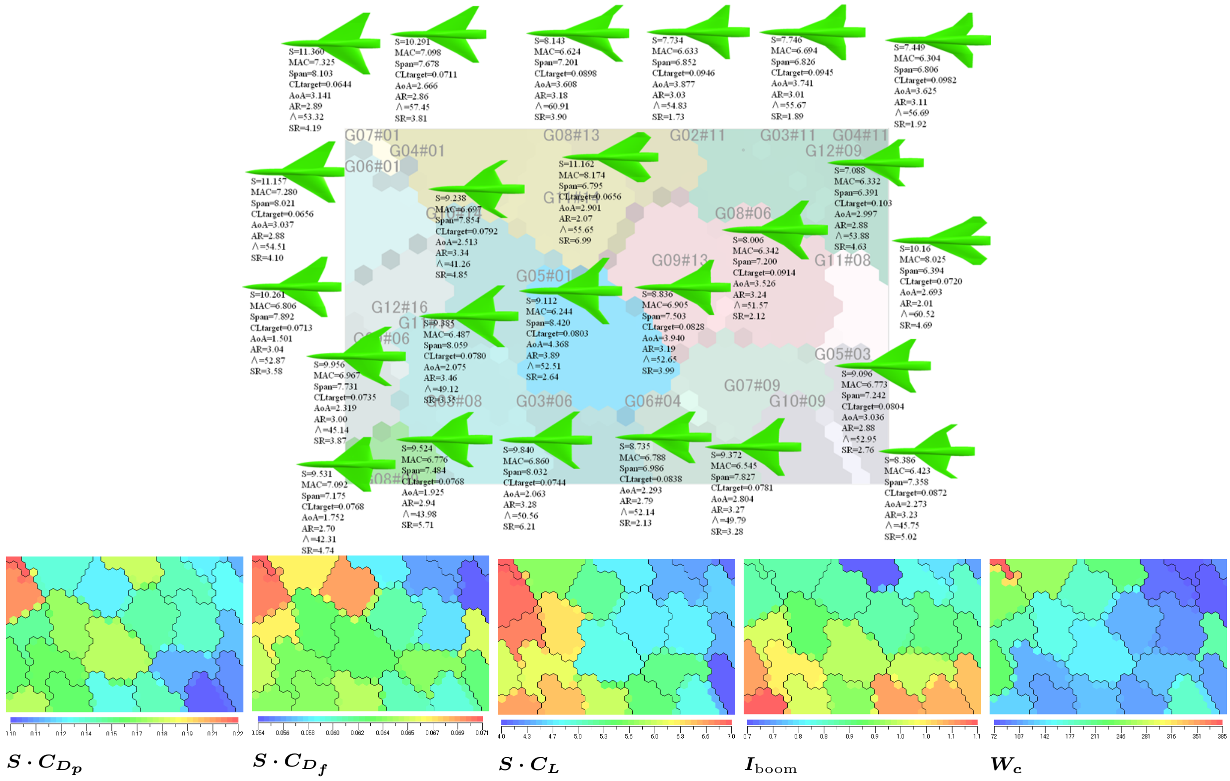

Figure 11. Derived SOM with the top views of sorted 24 individuals and their colored maps by the objective functions.

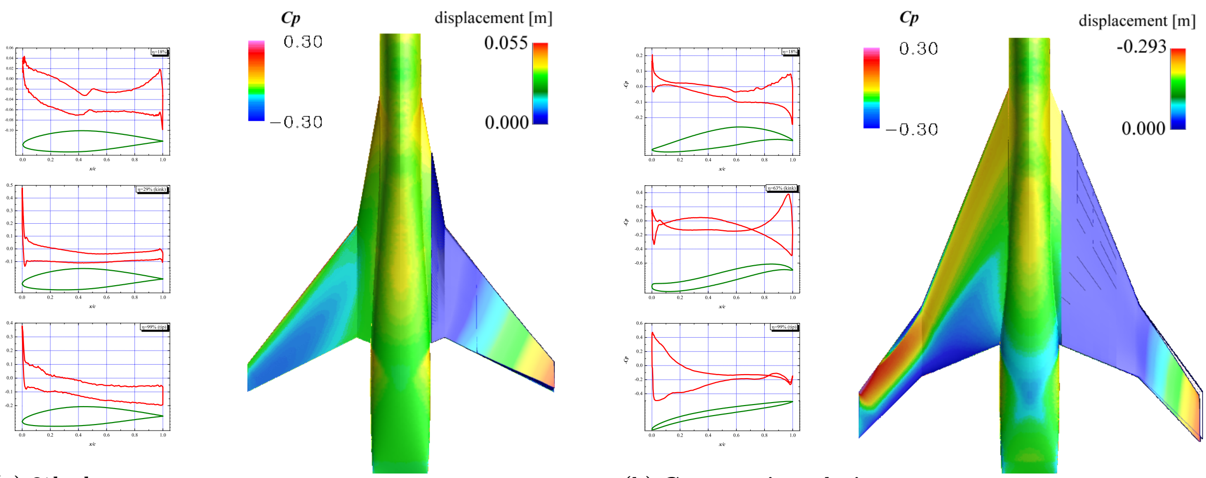

(a) 0th shape

(b) Compromise solution

Figure 12. Comparison of wing shape colored by C_p and displacement distributions, and C_p distributions near the junction relative to the fuselage, kink, and tip.

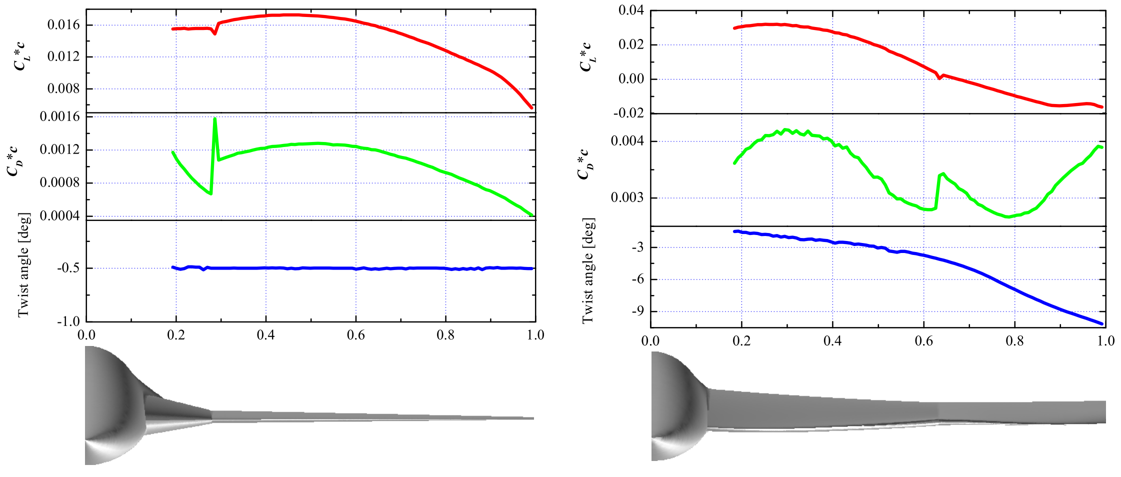

(a) 0th shape

(b) Compromise solution

Figure 13. Comparison of the spanwise distributions of C_L, C_D, and the twist angle.

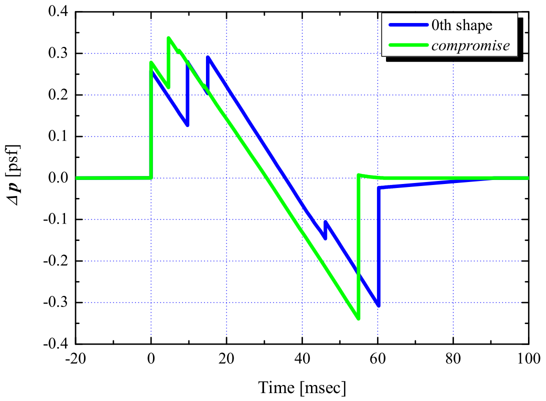

Figure 14. Comparison of ground pressure signatures.

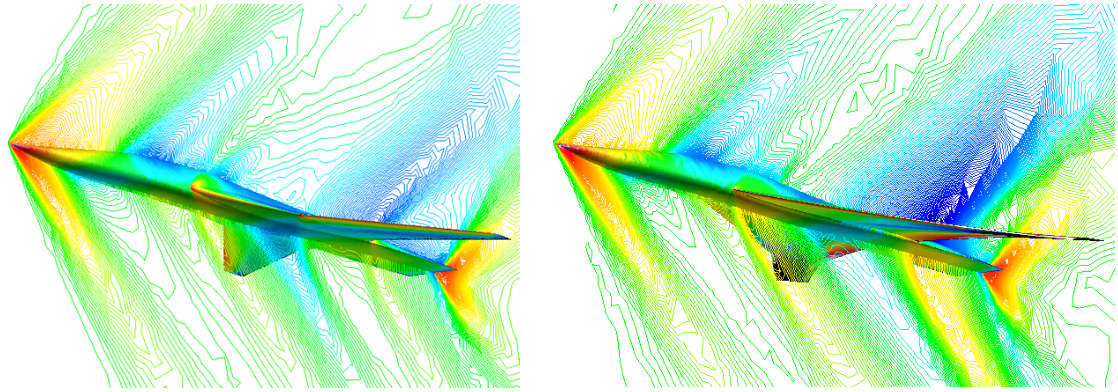

(a) 0th shape

(b) Compromise solution

Figure 15. Comparison of pressure distributions on symmetrical plane.

Table 3. **Comparison of geometrical characteristic values between 0th shape and *compromise* solution.**

Individual	$C_{L\,\mathrm{design}}$	α_{cruise}[deg]	AR	$S^{\mathrm{wetted}}_{\mathrm{wing}}[\mathrm{m}^2]$	$N^{\mathrm{ply}}_{\mathrm{out\_skin}}/N^{\mathrm{ply}}_{\mathrm{in\_skin}}/N^{\mathrm{ply}}_{\mathrm{in\_rib}}$
0th shape	0.132	2.33	3.81	10.41	8/72/24
compromise	0.0898	3.61	3.18	15.68	56/88/24

Table 4. **Comparison of the objective and aerodynamic-performance values between 0th shape and *compromise* solution.**

Individual	$S \cdot C_{D_p}$	(C_{D_p})	$S \cdot C_{D_f}$	$S \cdot C_L$	(C_L)	I_{boom}	W_c
0th shape	0.0656	(0.0118)	0.0482	3.896	(0.7029)	0.615	88.74
compromise	0.1777	(0.0218)	0.0584	4.719	(0.5794)	0.676	214.58

VI. Conclusions

The multidisciplinary design exploration for $\mathrm{S^3TD}$ wing has been performed using optimization and data mining taking five objective functions regarding aerodynamics, structures, and boom noise into consideration on PSO/GA hybrid method. Consequently, 12 generation was evolved and 75 non-dominated solutions were acquired. The knowledge in the design space was obtained regarding the tradeoffs and correlation among the objective functions. Furthermore, the particular design variables, which give effects on the objective functions, was revealed. The design knowledge is essential for successful decision of a compromise solution. The selected compromise solution improves in lift performance as well as the restraint of sonic boom intensity. Since wing area and planform shape give strong effects on the objective functions due to the definition of the present optimization problem, a next-step MDO will be carried out for practical design of wing cross-section geometry.

Acknowledgments

We would like to thank all members of the supersonic transport team in aviation program group, JAXA for providing useful advice. The Euler/NASTRAN computations were performed using the Central Numerical Simulation System of Numerical Simulator III in JEDI center, JAXA.

References

[1]Ohnuki, T., Hirako, K., and Sakata, K., "National Experimental Supersonic Transport Project," *Proceedings on 25th International Council of the Aeronautical Sciences*, ICAS 2006-1.4.1, Hamburg, Germany, 2006.

[2]Murakami, A., "Silent Supersonic Technology Demonstration Program," *Proceedings on 25th International Council of the Aeronautical Sciences*, ICAS 2006-1.4.2, Hamburg, Germany, 2006.

[3]Sasaki, D., Obayashi, S., and Nakahashi, K., "Navier-Stokes Optimization of Supersonic Wings with Four Objectives Using Evolutionary Algorithm," *Journal of Aircraft*, Vol. 39, No. 4, 2002, pp. 621–629.

[4]Chiba, K., Obayashi, S., Nakahashi, K., and Morino, H., "High-Fidelity Multidisciplinary Design Optimization of Aerostructural Wing Shape for Regional Jet," AIAA Paper 2005-5080, 2005.

[5]Ito, Y. and Nakahashi, K., "Direct Surface Triangulation Using Stereolithography Data," *AIAA Journal*, Vol. 40, No. 3, 2002, pp. 490–496.

[6]Kumano, T., Jeong, S., Obayashi, S., Ito, Y., Hatanaka, K., and Morino, H., "Multidisciplinary Design Optimization of Wing Shape for a Small Jet Aircraft Using Kriging Model," AIAA Paper 2006-0932, 2006.

[7]Kennedy, J. and Eberhart, R., "Particle Swarm Optimization," *Proceedings of the Fourth IEEE International Conference on Neural Networks*, 1995, pp. 1942–1948.

[8]Alvarez-Benitez, J. E., Everson, R. M., and Fieldsend, J. E., "A MOPSO Algorithm Based Exclusively on Pareto Dominance Concepts," *The 3rd International Conference on Evolutionary Multi-Criterion Optimization, LNCS 3410*, Springer-Verlag Heidelberg, Guanajuato, Mexico, 2005, pp. 459–473.

[9]Fonseca, C. M. and Fleming, P. J., "Genetic Algorithms for Multiobjective Optimization: Formulation, Discussion and Generalization," *Proceedings of the Fifth International Conference on Genetic Algorithms*, 1993, pp. 416–423.

[10]Obayashi, S., Takahashi, S., and Takeguchi, Y., "Niching and Elitist Models for MOGAs, Parallel Problem Solving from Nature," *The 5th International Conference onParallel Problem Solving from Nature, LNCS 1498*, Springer, Berlin, Heidelberg, New York, 1998, pp. 260–269.

[11]Simpson, T. W., Mauery, T. M., Korte, J. J., and Mistree, F., "Kriging Models for Global Approximation in Simulation-Based Multidisciplinary Design Optimization," *AIAA Journal*, Vol. 39, No. 12, 2001, pp. 2233–2241.

[12]Keane, A. J., "Statistical Improvement Criteria for Use in Multiobjective Design Optimization," *AIAA Journal*, Vol. 44, No. 4, 2006, pp. 879–891.

[13]Jeong, S., Murayama, M., and Yamamoto, K., "Efficient Optimization Design Method Using Kriging Model," *Journal of Aircraft*, Vol. 42, No. 2, 2005, pp. 413–420.

[14]Keane, A. J., "Wing Optimization Using Design of Experiment, Response Surface, and Data Fusion Methods," *Journal of Aircraft*, Vol. 40, No. 4, 2003, pp. 741–750.

[15]Eshelman, L. J. and Schaffer, J. D., "Real-Coded Genetic Algorithms and Interval Schemata," *Foundations of Genetic Algorithms 2*, Morgan Kaufmann, San Mateo, CA, 1993, pp. 187–202.

[16]Takahashi, M. and Kita, H., "A Crossover Operator Using Independent Component Analysis for Real-Coded Genetic Algorithms," *Proceedings of IEEE Congress on Evolutionary Computation 2001*, 2001, pp. 643–649.

[17]Obayashi, S. and Guruswamy, G. P., "Convergence Acceleration of an Aeroelastic Navier-Stokes Solver," *AIAA Journal*, Vol. 33, No. 6, 1994, pp. 1134–1141.

[18]Venkatakrishnan, V., "On the Accuracy of Limiters and Convergence to Steady State Solutions," AIAA Paper 93-0880, 1993.

[19]Sharov, D. and Nakahashi, K., "Reordering of Hybrid Unstructured Grids for Lower-Upper Symmetric Gauss-Seidel Computations," *AIAA Journal*, Vol. 36, No. 3, 1998, pp. 484–486.

[20]Obayashi, S. and Sasaki, D., "Visualization and Data Mining of Pareto Solutions Using Self-Organizing Map," *The 2nd International Conference on Evolutionary Multi-Criterion Optimization, LNCS 2632*, Springer-Verlag Heidelberg, Faro, Portugal, 2003, pp. 796–809.

[21]Holden, C. M. E. and Keane, A. J., "Visualization Methodologies in Aircraft Design," AIAA Paper 2004-4449, 2004.

[22]Chiba, K., Obayashi, S., and Nakahashi, K., "Design Exploration of Aerodynamic Wing Shape for Reusable Launch Vehicle Flyback Booster," *Journal of Aircraft*, Vol. 43, No. 3, 2006, pp. 832–836.

[23]Jones, D. R., Schonlau, M., and Welch, W. J., "Efficient Global Optimization of Expensive Black-Box Functions," *Journal of Global Optimization*, Vol. 13, No. 4, 1998, pp. 455–492.

[24]Kohonen, T., *Self-Organizing Maps*, Springer, Berlin, Heidelberg, 1995.

[25]Deboeck, G. and Kohonen, T., *Visual Explorations in Finance with Self-Organizing Maps*, London, Springer Finance, 1998.

[26]Pampalk, E., Rauber, A., and Merkl, D., "Content-Based Organization and Visualization of Music Archives," *Proceedings of the 10th International conference on Multimedie*, ACM Press, NY, 2002, pp. 570–579.

[27]Vesanto, J. and Alhoniemi, E., "Clustering of the Self-Organizing Map," *IEEE Transactions on Neural Networks*, Vol. 11, No. 3, 2000, pp. 586–600.